MICROROBOTS

Spatially selective remote magnetic actuation of identical helical micromachines

Jürgen Rahmer,[1]* Christian Stehning,[2] Bernhard Gleich[1]

Magnetic micromachines can be controlled remotely inside the human body by application of external magnetic fields, making them promising candidates for minimally invasive local therapy delivery. For many therapeutic scenarios, a large team of micromachines is required, but a convincing approach for controlling individual team members is currently missing. We present a method for selective control of identical helical micromachines based on their spatial position. The micromachines are operated by uniform rotating fields, whereas spatial selection is achieved by application of a strong field gradient that locks all machines except those located inside a small movable volume. We deliver experimental evidence of three-dimensional selective actuation with a spatial selectivity on the order of millimeters over a workspace large enough for clinical applications. Selective control of teams of helical micromachines may improve minimally invasive therapeutic approaches and may lead to more flexible local drug delivery systems or adaptive medical implants. As an example, we propose a concept for adaptive radiation treatment in cancer therapy based on selective switching of radioactive sources distributed inside a tumor.

INTRODUCTION

Magnetic fields are used in many contexts to apply torques and forces for remote control of magnetic devices. In medical applications, they navigate a catheter inside the heart (*1*) or steer a video capsule in the gastrointestinal tract (*2*). Magnetic devices can be miniaturized, as scaling laws predict constant ratios of torque to volume and force to volume, respectively (*3*). Thus, magnetic control has been demonstrated with objects as small as a few micrometers (*4*–*6*). High potential is seen in micromachines for local therapy delivery (*7*, *8*), and various designs for magnetic micromachines have been proposed (*9*–*11*). However, many promising applications, such as homogeneous local drug delivery, require the control of many micromachines for distributed operation on the same task (*12*). Although "swarm control" has been demonstrated by simultaneous steering of identical micromachines using a uniform field (*13*), individual control of members of a team of micromachines, that is, "multirobot control," remains a challenge (*14*). To date, only small numbers of micromachines can be controlled individually, and they need to differ in their magnetism or mechanical composition (*15*–*17*). We introduce a concept for controlling selected members of a team of identical helical micromachines based on their spatial position. The method combines a static magnetic field gradient with the application of dynamic uniform fields. The gradient field, also called the selection field, selects a small volume by locking the actuation of all machines located outside this volume. The dynamic fields are used to position that volume on the desired machine(s) and to perform the actuation. The concept is inspired by the field configuration used for signal localization in magnetic particle imaging (MPI) (*18*). Proof-of-principle experiments have been performed using MPI field generators because of their ability to generate the required field configurations (*19*, *20*). However, the magnetic manipulation concept is completely independent of MPI and, depending on application scenario, can be realized with simpler dedicated field applicators.

[1]Philips GmbH Innovative Technologies, Research Laboratories, Röntgenstraße 24-26, 22335 Hamburg, Germany. [2]Philips GmbH Market DACH, Röntgenstraße 22, 22335 Hamburg, Germany.
*Corresponding author. Email: juergen.rahmer@philips.com

Figure 1 (A and B) displays a sketch and a photograph of a field applicator with a bore diameter of 12 cm. It consists of three pairs of coils mounted along the three spatial axes and cylindrical soft magnetic cores for field amplification in z direction. If a coil pair is driven with parallel currents of equal amplitude, it creates a spatially uniform field along the axis, similar to a Helmholtz coil. The combination of three coil pairs enables the generation of uniform dynamic fields with arbitrary orientation. In z direction, the currents can be adjusted individually for each coil. If the currents have the same amplitude but opposite signs, the coil pair acts as a Maxwell coil (*21*) that creates a uniform selection field gradient in the vicinity of the center of the setup, as shown in Fig. 1C. Because of the symmetry of the setup, the field is zero at the center point, which is therefore called the field-free point (FFP). Concurrent application of the selection field gradient and dynamic uniform fields leads to a field superposition. It can be described locally (by looking at the resulting field variation at a fixed spatial position) or globally (by looking at the resulting FFP shift in space). Both views have advantages in certain circumstances. As further detailed in Materials and Methods, in the global view, any dynamic sequence of uniform fields applied in the presence of the static gradient field can be translated into a unique spatial trajectory that the FFP traverses in time. Within a limited volume around the center of the field generator, the relation between applied uniform field strength and FFP translation is approximately linear. Expressing a field sequence in terms of an FFP trajectory can be useful for understanding and designing manipulation sequences for micromachines.

RESULTS

Consider many identical screws distributed over a three-dimensional (3D) volume at random positions and orientations (Fig. 2A). Each screw resides in a threaded cylinder that is fixed in space. The screw can be moved inside the cylinder by rotation about its long axis. It further contains hard magnetic material that is magnetized transversely to its axis of rotation. Our objective is to actuate each screw individually by applying external magnetic fields, that is, to drive it forward or backward without driving any of the other screws.

When an external magnetic field is applied transversely to the screw axis, but at an angle with respect to the magnetization vector,

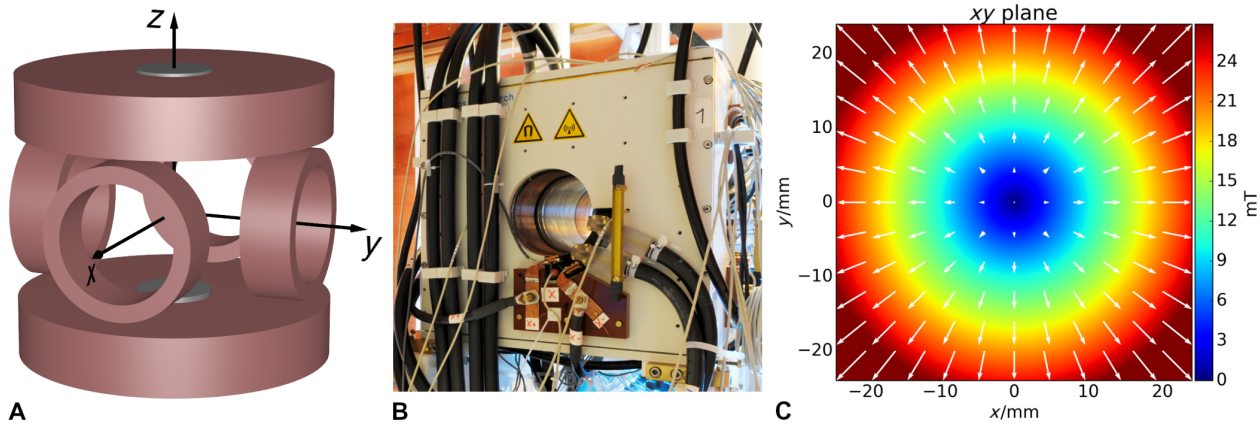

Fig. 1. Field generator and FFP. (**A**) Schematic of field generator, consisting of three orthogonal sets of coils (copper color) and an iron core in *z* direction (gray color). Each coil pair in *x* and *y* direction is driven by an individual amplifier in a Helmholtz configuration and thus generates a spatially uniform field. In *z* direction, each coil is supplied by an individual amplifier so that all field configurations between a Helmholtz (same current amplitudes and signs on both coils) and a Maxwell configuration (same current amplitudes but opposite signs) can be generated. The Maxwell configuration generates a spatially uniform selection field gradient. (**B**) Photograph of the field generator. The bore diameter is 12 cm. (**C**) Idealized selection field generated in the Maxwell configuration at the center of the field generator. An *xy* plane through the center of the setup is shown. Its center point is the position of the FFP, where the field magnitude (color map) is zero. White arrows represent local field vectors.

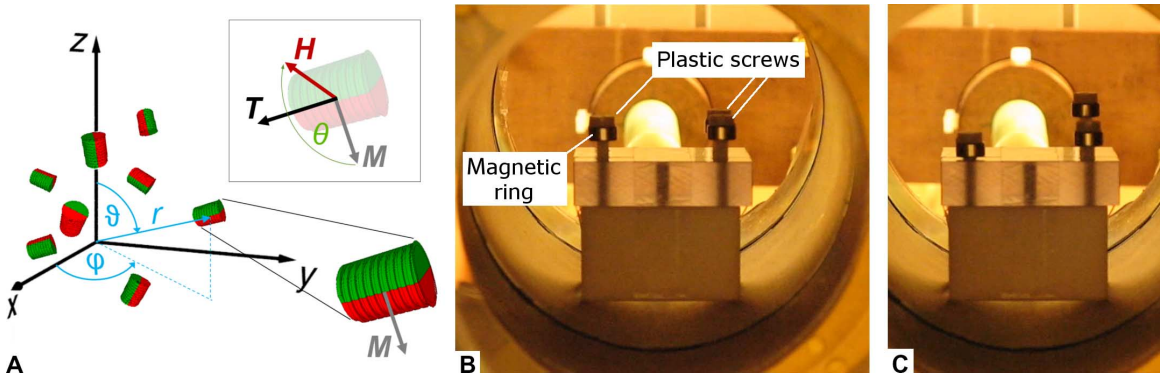

Fig. 2. Three-dimensional arrangement of screws and spatially selective actuation demonstration. (**A**) General scenario of randomly distributed screws. In spherical coordinates, a screw position is determined by its distance from the origin *r*, azimuth φ, and polar angle ϑ. The magnetization vector of a screw **M** is oriented transversely to the screw axis. If a magnetic field **H** is applied in the plane transverse to the axis as well, a torque **T** is generated about the axis (inset). (**B**) Three plastic screws mounted in a threaded plate are equipped with magnetic rings with magnetization orientation transverse to the screw axes. Application of a rotating uniform field in the horizontal plane drives all screws simultaneously. (**C**) Superposition of a strong gradient field on the rotating field allows driving selected screws individually (movie S1).

a torque is created that causes the screw to turn (Fig. 2A, inset). If the field rotates about the axis, the screw can be driven continuously in its thread. However, when applying a uniform rotating field $\mathbf{H}_{\mathrm{rot}}(t)$ to a distribution of screws, all screws sharing the correct alignment with respect to the applied field will follow the rotation. To gain control over an individual screw, the rotating field needs to be confined to a small volume around it. We achieve this by applying a static selection field $\mathbf{H}_{\mathrm{s}}(\mathbf{r})$, whose dependence on spatial position **r** has a linear gradient in each field component. If no other fields are applied, the FFP is located at the center of the setup, that is, $\mathbf{H}_{\mathrm{s}}(0) = 0$. In the combined field, $\mathbf{H}(\mathbf{r}, t) = \mathbf{H}_{\mathrm{s}}(\mathbf{r}) + \mathbf{H}_{\mathrm{rot}}(t)$, a screw located at the FFP will only experience the rotating field component and will follow the rotation if its axis is correctly aligned. However, when moving away from the FFP, the static component increases almost linearly and soon becomes larger than the rotating component. In that case, depending on the orientation between the two field components, the total field vector either does not rotate or exerts a tilting torque on the screw axis. We assume here that the microdevices reside in a sufficiently rigid environment, so the tilting torque blocks screw rotation inside the thread (details in Materials and Methods). Consequently, the field configuration selectively drives screws located in a small volume around the FFP, whereas all other screws are locked by the local static field. To sequentially center this actuation volume on different screw positions, an additional uniform offset field $\mathbf{H}_{\mathrm{offs}}(t)$ is applied. Knowledge about the position and orientation of the screws can be obtained using a 3D imaging method, for example, x-ray computed tomography (*22*).

For a simple demonstration, let us first look at three screws positioned inside the bore of our field applicator (Fig. 2B). Attached to each screw is a magnetic ring whose magnetization is oriented perpendicularly to the screw axis. A screw is a helical object, and helical objects can be driven by a uniform rotating field $\mathbf{H}_{\mathrm{rot}}(t)$ (*11*). In that case, all screws simultaneously move up or down, depending on the sense of field rotation. With a uniform field, the screws cannot be operated individually. To address individual screws, we need to superimpose a selection field $\mathbf{H}_{\mathrm{s}}(\mathbf{r})$ that locks the rotation of all screws except for the one located at the FFP position. With the help of an offset field $\mathbf{H}_{\mathrm{offs}}(t)$, this enables the selection of

a single screw for rotation, whereas the others do not follow (Fig. 2C and movie S1). The field sequence can be visualized by looking at the resulting FFP trajectory. Figure 3A shows the field configuration in the central *xy* plane, where the screws are located. The static selection field component $\mathbf{H}_s(\mathbf{r})$ generates the FFP that is moved to a screw position by $\mathbf{H}_{offs}(t)$ (position of the red arrow with white outline). At the FFP, the screw is subject only to the rotating field $\mathbf{H}_{rot}(t)$. The field plot in Fig. 3A shows that the rotating field component causes the FFP to travel along a circular trajectory around the screw position (red circle). Field vectors inside the circle fulfill a complete rotation (red arrows), whereas field vectors outside do not rotate (movie S3). If a single screw is to be selected for actuation, the radius of the circular FFP path $r_{FFP} = \|\mathbf{H}_{rot}(t)\|/G_x$ has to be adjusted so that the circle encloses only the desired screw. Hereby, $G_x = G_y$ is the gradient strength in the *xy* plane. To actuate a subset of screws, the amplitude of the rotating field can be increased or the gradient can be lowered so that more screws are encircled by the FFP path. The field amplitude can even be changed during rotation to generate a noncircular closed path around the objects to be included in the actuation.

For an application-related experiment, we prepared smaller screws that operate in threaded plastic cylinders (Fig. 4). These can be seen as models for switchable radioactive sources to be implanted into tumors for radiation therapy, so-called seeds (*23*). For switching a seed off and on, the radioactive material attached to the screw would be moved in and out of a cylinder made from radiopaque metal. In the model seeds, radioactivity is represented by optically phosphorescent material (Fig. 4A).

For demonstration of horizontally selective actuation, we performed a planar experiment with four model seeds positioned at the corners of a square in the bore of a field generator (Fig. 4B). As the screw axes were aligned vertically (*z* direction), a rotating field was applied in the horizontal (*xy*) plane for actuation. At the beginning of the sequence, the rotating field was applied in the absence of a gradient field so that all screws were driven simultaneously into their thread and the optical emission was shielded. In the next step, the sense of rotation was reversed, and a static gradient field was added in conjunction with static offset fields that centered the FFP sequentially

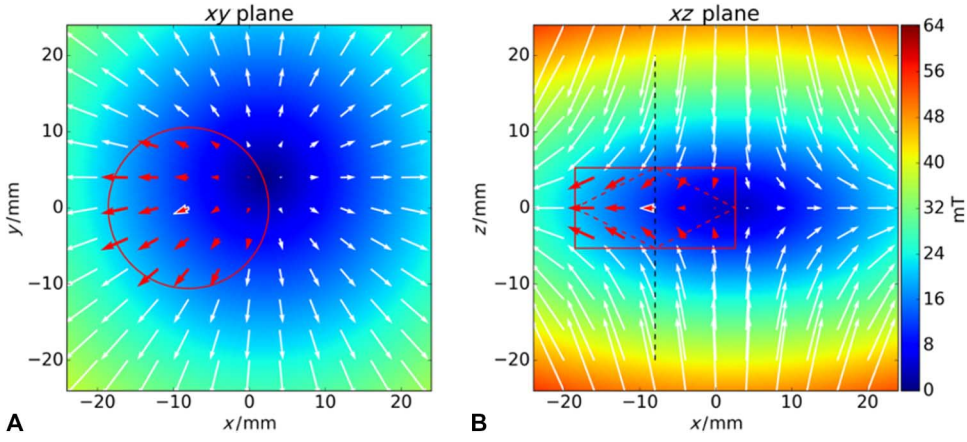

Fig. 3. Field configuration for spatially selective actuation of helical objects with axis transverse to the horizontal (*xy*) plane. (**A**) The static gradient field generates an FFP in the *xy* plane (dark blue area). Arrows indicate local field vectors, whereas background color represents field magnitude. Application of a rotating horizontal field component moves the FFP on a circular path (red circle) (movie S3). All positions inside the circle experience a rotating field (red arrows), whereas outside the circle, the field vectors do not go through a full rotation. Thus, actuation of helical objects can be confined to the circle. The central arrow (red with white outline) experiences a constant torque, whereas the other red arrows are subject to a variable torque. (**B**) Field configuration in the *xz* plane. The black dashed line indicates the orientation of the helical axis for optimal rotation. The red box is a projection of the cylinder to which actuation is confined under the assumption of a minimal tilting torque required to prevent rotation. The red dashed diamond shape is a projection of the double-cone volume to which actuation is confined under the assumption of a minimal field angle at which rotation is blocked (see Materials and Methods).

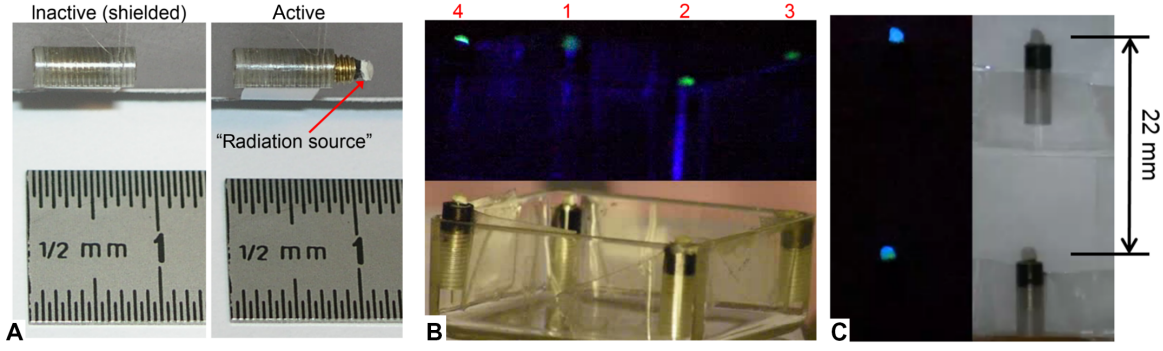

Fig. 4. Switchable radiation source demonstrators and experimental verification of 3D spatially selective actuation. (**A**) The "radiation source" (a phosphorescent powder) is placed at the tip of a brass screw filled with hard magnetic material. The magnetic moment is transverse to the screw axis. To switch off the source, rotating magnetic fields drive the screw into the threaded plastic cylinder that shields the "radiation." (**B**) For the demonstration of horizontal selectivity, four switchable sources are mounted at the corners of a quadratic rectangle with edge length of 26 mm, which is positioned in the bore of the field applicator. The sequence is applied two times, once with illumination (bottom) and once without illumination to visualize the "radiation sources." In the first part of the sequence, the seeds are switched off jointly by application of a rotating field with amplitude of 7.5 mT/μ_0. In the second part, the sense of rotation is reversed, and a field gradient of $G_x = G_y = 0.5$ T/m/μ_0 is superimposed to selectively switch on the seeds. As a consequence, the FFP travels on a circular path of 15-mm radius (cf. Fig. 3), which is small enough to reliably avoid actuation of neighboring screws. Using an additional offset field, the actuation volume is successively placed on each screw, in the order indicated by the numbers (movie S2). (**C**) For the demonstration of vertical selectivity, the sources are mounted above each other. In that case, a gradient of $G_x = G_y = 1.25$ T/m/μ_0 is applied, whereas the amplitude of the rotating field component is 25 mT/μ_0. First, the lower source is switched off by centering the FFP trajectory around its screw. Second, it is centered on the upper screw to switch off the upper source. Finally, both are switched on jointly by applying the rotating field sequence in the absence of a gradient (movie S4).

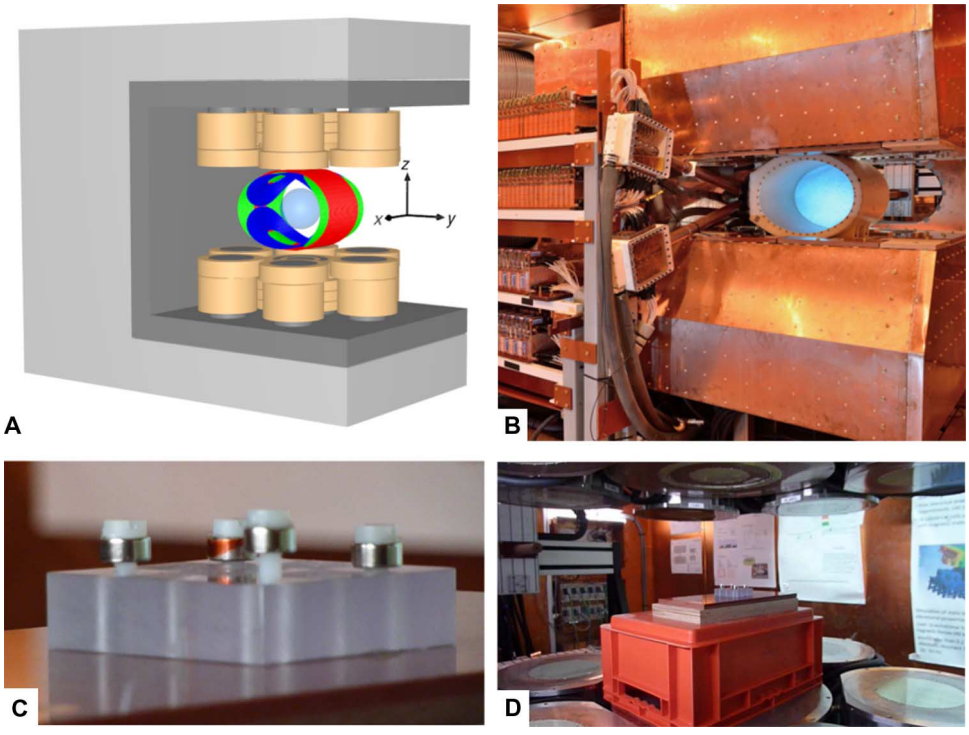

Fig. 5. Spatially selective actuation experiment on clinical-scale field applicator. (**A**) Schematic of field generator, consisting of a total of 16 coil stacks (copper color) mounted on a steel yoke (light gray). Soft magnetic materials are used for flux guidance (dark gray). The central coils colored in red, green, and blue are high-frequency coils used for MPI and have not been used in the manipulation experiments. The sphere at the center indicates the spherical volume over which the FFP can be shifted while maintaining a gradient strength of G_z = 2.0 T/m/μ_0. It has a diameter of 20 cm. Outside this volume, selective actuation is also possible with increasingly lower spatial selectivity. (**B**) Photograph of field generator with high-frequency coils and copper shielding installed. The bore diameter of the high-frequency coils is 34 cm and 45 cm in vertical and horizontal direction, respectively. (**C**) Demonstration of spatially selective actuation on clinical-scale system. The experiment is similar to the one shown in Fig. 2 (B and C). Three of the four screws are driven up and down individually during the field sequence (see movie S7). (**D**) Overview image of the screws placed at the center of the field generator. When the imaging coils and the copper shielding required for imaging are not mounted, the accessible space has a height of 42 cm and is open laterally.

on the four screws. This procedure allowed individual operation of all screws, which were sequentially driven upward until the phosphorescent source was visible again (movie S2). The achievable spatial selectivity of the method depends on the available gradient strength and the minimal torque required to drive the screw. For our field generators and model screws, a conservative estimate yields a maximum spatial selectivity, that is, minimal screw separation for individual actuation, between 3 and 4 mm (see Materials and Methods).

Looking at the field configuration in the *xz* plane (Fig. 3B), one finds that screws located above or below the disc encircled by the FFP path also experience a rotating field component. However, outside the plane of FFP motion, the increasing vertical field component creates a tilting torque on the screw axis and thus increases friction. At a certain magnitude of the vertical field component, friction is large enough to block screw rotation. This mechanism constrains the actuation volume to a cylinder, whose length is determined by the minimal vertical field required to block the screw. The projection of this cylinder is displayed in Fig. 3 (A and B) (red circle and solid rectangle, respectively). For demonstration of vertically selective actuation, two model seeds were placed coaxially above each other (Fig. 4C) so that the same lateral field components apply. First, the lower screw was driven into its cylinder by placing the plane of FFP motion at its level. In that plane, the screw does not experience a tilting torque, whereas the screw located above the plane is subject to a strong tilting torque that blocks its rotation. In the next step, the upper screw was actuated by moving the plane to its level. Finally, both screws were jointly driven upward by switching off the gradient field and reversing the sense of rotation (movie S4). The feasibility of 3D selective actuation in a rigid environment is herewith demonstrated.

DISCUSSION

A point that needs to be considered is the force acting on magnetic micromachines in a magnetic field gradient. In the described medical application scenario, the screws are held in place by threaded cylinders embedded in capsules or implants that would be fixed by surrounding tissue. One can estimate that the magnetic forces would not exceed the weight of the implant and thus would not pose a risk in in vivo applications (see Materials and Methods). Tissue can resist even higher forces so that applications, where screws are directly driven through tissue (*24*), could also be combined with spatial selectivity. On the other hand, the permanent presence of forces on all objects in the workspace requires more effort when applying the selective actuation approach to magnetic swimmers in fluids (*5*). To achieve selective control over microswimmers, field sequences with high rotation frequency are necessary to keep the rotation-induced propulsion speed above the force-induced drift. In addition, rotation above or below the plane of FFP motion cannot be blocked by a tilting torque because the microswimmer would just realign with the field. However, the new orientation would require rotation about an axis different from the long axis of the helical device, which would be inefficient. Thus, one can expect that spatially selective actuation would work in fluids as well, but workable implementation strategies still need to be developed.

Attractive applications can already be realized with micromachines that reside in a rigid environment. One class of applications is based on mechanisms driven by several screws that are controlled individually. In orthopedics, this could be implants, whose shape can be adapted to the healing process or to correct inaccurate placement without the need for multiple motors or a power supply inside the device (*25*). In applications such as limb lengthening or early-onset scoliosis, a mechanism based on several controllable screws may offer higher flexibility in extendible prostheses or growth rods than currently available methods (*26*, *27*). In addition, the approach can be useful in microfluidics, where simple and tiny magnetic pumps and valves may be envisioned that can be individually actuated without an electrical or mechanical link. Another class of applications is related to simple

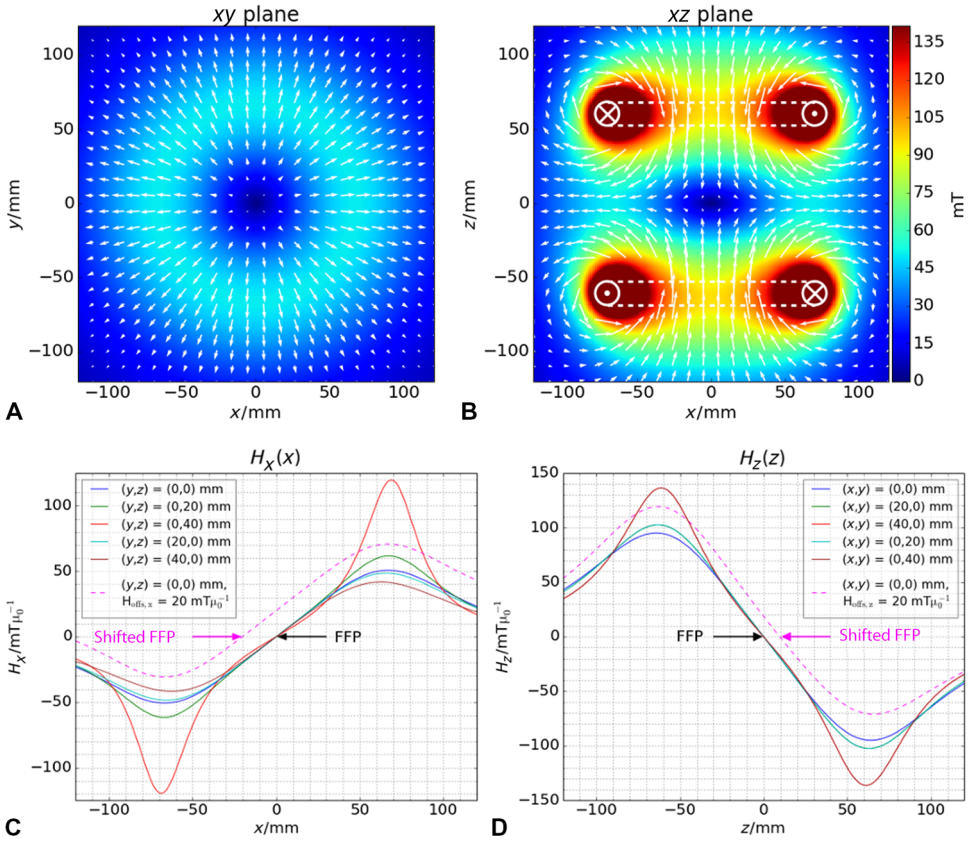

Fig. 6. Simulated field configuration of an ideal Maxwell coil. (**A**) Local field vectors (white) and absolute field values (color-coded) in the central *xy* plane. (**B**) Local field vectors (white) and absolute field values (color-coded) in the central *xz* plane. The coils are indicated by white dashed lines. For the field simulation, two circular coils with a radius of $R = 70$ mm, 120 windings, and a distance of $\sqrt{3}R \approx 121$ mm were supplied with a current of 100 A. At the center of the setup, the resulting gradient in the $H_z(\mathbf{r})$ field component points in *z* direction and has an amplitude of $G_z = -2.0$ T/m/μ_0. In the *xy* plane, gradients in the $H_x(\mathbf{r})$ and $H_z(\mathbf{r})$ components point along *x* and *y* and have amplitudes of $G_x = G_y = 1.0$ T/m/μ_0, respectively. (**C**) Linear field profiles of *x* field component $H_x(\mathbf{r})$ along *x* center line and along lines with lateral offsets in *y* and *z* direction. The slope of the field and thus the gradient G_x is uniform over about ±40 mm in each direction. At the FFP, the field is zero. Application of a uniform offset field leads to a linear shift of the FFP in space (pink dashed line). (**D**) Linear field profiles of *z* field component $H_z(\mathbf{r})$ along *z* center line and along lines with lateral offset in *x* and *y* direction. The slope of the field and thus the gradient G_z is uniform over about ±40 mm in each direction. Application of a uniform offset field thus leads to a linear translation of the FFP (pink dashed line).

micromachines for local therapy delivery, such as remote-controlled drug release from a distribution of injectable magnetic micropills (*28*). Remotely switchable radioactive seeds are a special case of this class. Compared to external beam radiation therapy, implantation of radioactive seeds into a tumor ["brachytherapy" (*23*)] avoids many side effects resulting from irradiating surrounding healthy tissue (skin irritations and bleeding) and reduces the risk of creating a radiation-induced second cancer. Despite these advantages, brachytherapy is currently applied only to few tumor types: Without the possibility of adjusting the seed radiation after implantation, the number of radioisotopes with a suitable decay half-life and radiation energy is limited. Furthermore, many tumors are hard to access for seed implantation. Switchable seeds would enable the use of sources with longer half-life or higher dose rates because the radiation can be switched off after the desired dose has been applied. Besides, migrating seeds ending up too close to healthy tissue or sensitive organs could be switched off. Using a helically slotted shield, directional seeds with remotely adjustable radiation direction could be built. These would allow further improvements in dose painting and sparing of healthy tissue (*29*, *30*). In addition, magnetic manipulation has been shown to be scalable to the micrometer regime (*3*, *11*). We estimate that the size of switchable radioactive seeds can be reduced to about 150 μm while maintaining the required thickness of the shield (for ^{103}Pd radiation). Using a catheter, seeds of this size could be discharged into the bloodstream of a tumor-feeding artery so that they are carried into the tumor and embolize small vessels. After localization via imaging, only seeds that ended up in the tumor would be activated remotely. To date, without the possibility of switching seeds, the approach is restricted to liver treatment ("selective internal radiation therapy"), where anatomy ensures that a large fraction of the seeds ends up in the tumor (*31*). Transarterial delivery of switchable seeds would make most tumors accessible for brachytherapy.

The selective actuation mechanism was demonstrated using a simple field applicator with six coils operated by four individual amplifiers, addressing three orthogonal uniform fields and a uniform gradient field in one spatial direction. The low complexity enables scaling of the field applicator to clinical size without substantially sacrificing field or gradient strength. Figure 5 (A and B) shows a clinical-scale field applicator. Here, a different coil configuration has been chosen for the field generator to enable patient access from the sides. Joint operation of several coil stacks containing soft magnetic cores generates the required uniform fields in all spatial directions. The maximum field gradient achieved in vertical direction is comparable to the maximum on the small system and is maintained while the FFP is moved inside a sphere with a diameter of 20 cm. Selective actuation is possible over an even larger workspace at reduced spatial selectivity. For demonstration, the selective manipulation experiment of Fig. 2 (B and C) has been repeated with this system (see Fig. 5C). If the imaging coils and shielding are mounted (Fig. 5B), the accessible work space has a height of 34 cm and a width of 45 cm; otherwise, the height limitation is 42 cm and the system is open laterally (movie S7).

In a clinical application, magnetic micromachines would need to be localized inside the human body before actuation. One approach would be to combine existing imaging equipment, such as cone beam computed tomography, with a simple open and mobile magnetic field applicator. The drawback is the use of ionizing radiation, which can be a limiting factor if continuous device monitoring is required. An alternative would be the use of MPI for localization. MPI is a highly

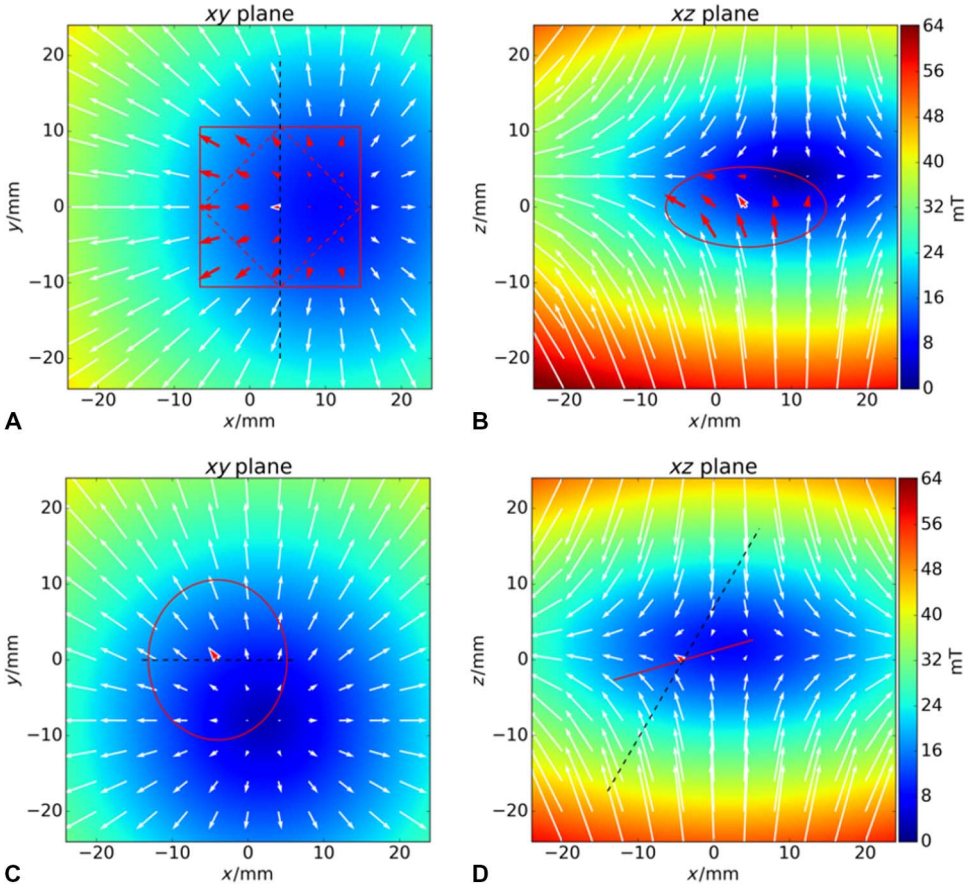

Fig. 7. Field configuration for spatially selective operation of helical objects with axis transverse to the *xz* plane (top row) and with oblique axis (ϑ = 30°, bottom row). (**A**) Axis for optimal rotation (black dashed line) and projection of actuation volumes under the assumption of a minimal blocking torque amplitude (cylinder, red quadratic rectangle) and minimal blocking torque angle (double cone, red dashed rectangle), respectively. (**B**) Because of the different gradient strengths in *x* and *z* direction, the FFP path is elliptical. The different gradient sign in *z* direction further leads to an opposite sense of rotation of the field components with respect to the FFP path (movie S5). (**C**) Projection of axis for optimal rotation (black dashed line) and projection of FFP path (red ellipsis) for actuation of screws with a polar angle of ϑ = 30° toward the *z* axis. (**D**) Axis for optimal rotation (black dashed line) and projection of FFP path (red line). Note that the plane of FFP motion and the optimal screw axis direction are no longer orthogonal (movie S6).

sensitive imaging method that is capable of quantitative 3D real-time imaging of iron oxide nanoparticles administered to the bloodstream (*32*). By labeling devices with MPI-visible markers, it can be used for catheter tracking (*33*, *34*) or image-guided closed-loop steering of untethered magnetic devices (*20*). Hence, it could also localize microdevices by visualizing either their markers or the intrinsic artifact created by their magnetism. Because MPI is a magnetic imaging technique, ferromagnetic objects create artifacts in imaging. For soft magnetic millimeter-sized objects, the artifacts extend only slightly beyond the objects (*20*). For hard magnetic FeNdB material, a thin copper shield would probably be necessary around the magnetic object to avoid the generation of unwanted signal harmonics by the excitation field operating in the kilohertz range. MPI and magnetic manipulation can, in principle, be performed concurrently (*20*), but imaging and manipulation sequences are not independent and may require some compromises, for example, interleaving imaging and manipulation. Overall, MPI is principally suited for the localization of small ferromagnetic objects, resulting in an attractive scenario: a highly versatile field applicator integrating a fast 3D imaging method that is capable of operating at the clinical scale without the use of ionizing radiation.

MATERIALS AND METHODS

Field configuration

The required field configuration $\mathbf{H}(\mathbf{r}, t)$ has three components,

$$\mathbf{H}(\mathbf{r},t) = \mathbf{H}_{\mathrm{s}}(\mathbf{r}) + \mathbf{H}_{\mathrm{offs}}(t) + \mathbf{H}_{\mathrm{rot}}(t) \quad (1)$$

where $\mathbf{H}_{\mathrm{s}}(\mathbf{r})$ represents the static gradient field or selection field, and $\mathbf{H}_{\mathrm{offs}}(t)$ and $\mathbf{H}_{\mathrm{rot}}(t)$ represent the dynamic uniform fields used for moving the FFP to the object location and for applying the rotating field, respectively.

For generation of these field components, the simplest approach is to use three orthogonal coil pairs. Operated in Helmholtz configuration, uniform fields of arbitrary orientation can be generated. By applying opposite currents to the coils in *z* direction, a Maxwell configuration that produces a uniform field gradient is realized. Application of different current amplitudes to the two coils leads to a superposition of uniform fields and a uniform field gradient. For illustration, Fig. 6 (A and B) displays the field configuration of a Maxwell coil aligned with the *z* axis in the central *xy* and *xz* plane, respectively. The coils have a radius of R = 70 mm and a distance of $\sqrt{3}R \approx 121$ mm. The field vanishes at the symmetry center, the location of the FFP. Figure 6C shows profiles of the *x* field component $H_x(\mathbf{r})$ along the *x* direction. The profiles were also calculated at positions with a lateral offset in *y* and *z* direction, respectively. One finds that the *x* component of the field gradient, $\mathbf{G}_x(\mathbf{r}) = \nabla H_x(\mathbf{r})$, is uniform over about 40 mm in each direction around the center of the system. Figure 6D shows that the same is true for $H_z(\mathbf{r})$. Therefore, inside the center volume, the gradients in each field component can be approximated as follows:

$$\mathbf{G}_x(\mathbf{r}) = \nabla H_x(\mathbf{r}) \approx \begin{pmatrix} G_x \\ 0 \\ 0 \end{pmatrix}, \quad \mathbf{G}_y(\mathbf{r}) = \nabla H_y(\mathbf{r}) \approx \begin{pmatrix} 0 \\ G_y \\ 0 \end{pmatrix},$$

$$\mathbf{G}_z(\mathbf{r}) = \nabla H_z(\mathbf{r}) \approx \begin{pmatrix} 0 \\ 0 \\ G_z \end{pmatrix} \quad (2)$$

When a parallel current contribution is added, a coil pair generates a field component that is uniform over the center volume, for example, $\mathbf{H}(\mathbf{r}) = (H_x, 0, 0)^T$ for the *x* coils. As shown in Fig. 6 (C and D), uniform

fields have the effect of shifting the FFP linearly in space, that is, $\Delta x = H_x/G_x$ for the uniform field applied in x direction in Fig. 6C.

Over the extent of the workspace, the static field can thus be approximated by the linear expansion about the symmetry center of the setup

$$\begin{aligned}\mathbf{H}_s(\mathbf{r}) &\approx \begin{pmatrix} \frac{\partial H_x(\mathbf{r})}{\partial x} & \frac{\partial H_x(\mathbf{r})}{\partial y} & \frac{\partial H_x(\mathbf{r})}{\partial z} \\ \frac{\partial H_y(\mathbf{r})}{\partial x} & \frac{\partial H_y(\mathbf{r})}{\partial y} & \frac{\partial H_y(\mathbf{r})}{\partial z} \\ \frac{\partial H_z(\mathbf{r})}{\partial x} & \frac{\partial H_z(\mathbf{r})}{\partial y} & \frac{\partial H_z(\mathbf{r})}{\partial z} \end{pmatrix} \begin{pmatrix} x \\ y \\ z \end{pmatrix} \\ &= \begin{pmatrix} \mathbf{G}_x(\mathbf{r}) & \mathbf{G}_y(\mathbf{r}) & \mathbf{G}_z(\mathbf{r}) \end{pmatrix}^T \begin{pmatrix} x \\ y \\ z \end{pmatrix} \\ &\approx \begin{pmatrix} G_x & 0 & 0 \\ 0 & G_y & 0 \\ 0 & 0 & G_z \end{pmatrix} \begin{pmatrix} x \\ y \\ z \end{pmatrix} \\ &= \begin{pmatrix} -\frac{G_z}{2} & 0 & 0 \\ 0 & -\frac{G_z}{2} & 0 \\ 0 & 0 & G_z \end{pmatrix} \begin{pmatrix} r\cos\varphi\sin\vartheta \\ r\sin\varphi\sin\vartheta \\ r\cos\vartheta \end{pmatrix} = \mathbf{G}\,\mathbf{r} \end{aligned} \tag{3}$$

where G_x, G_y, and G_z are the gradient strengths in the respective field components. The relation $G_z = -2G_x = -2G_y$ holds for a Maxwell coil field generator that is aligned with the z axis and has some distance to the workspace (*35*). In a second step, the Cartesian coordinates have been replaced by spherical coordinates with radial distance to the symmetry center of the setup r, polar angle ϑ, and azimuthal angle φ, as shown in Fig. 2A.

Because of the anisotropy of the gradient field, the field magnitude depends on both the distance from the FFP r and the polar angle ϑ:

$$\|\mathbf{H}_s(\mathbf{r})\| = \frac{G_z r}{2}\sqrt{1 + 3\cos^2\vartheta} \tag{4}$$

Torques and requirements for rotation

Consider a hard magnetic object located at position $\mathbf{r}_0$, which has a magnetic moment $\mathbf{m}$ given by the product of its volume V and remanent magnetization $\mathbf{M}$. In an applied field $\mathbf{H}(\mathbf{r},t)$, it experiences a torque

$$\mathbf{T}(\mathbf{r}_0,t) = \mu_0\,\mathbf{m} \times \mathbf{H}(\mathbf{r}_0,t) = \mu_0 V \mathbf{M} \times \mathbf{H}(\mathbf{r}_0,t) \tag{5}$$

Suppose that the magnetic object is helical, for example, a screw, and that its magnetization vector is transverse to its axis of rotation. For rotation, the applied field has to fulfill two requirements. First, the torque acting on the screw should be colinear with its axis; otherwise, the axis would be tilted into a new orientation. This requires the cross product between unit axis vector $\mathbf{n}_{ax}$ and torque to be zero,

$$\begin{aligned}\mathbf{n}_{ax} \times \mathbf{T}(\mathbf{r}_0,t) &= \mu_0 \mathbf{n}_{ax} \times \Big(\mathbf{m} \times \mathbf{H}(\mathbf{r}_0,t)\Big) \\ &= \mu_0 \Big(\Big(\mathbf{n}_{ax} \cdot \mathbf{H}(\mathbf{r}_0,t)\Big)\mathbf{m} - (\mathbf{n}_{ax} \cdot \mathbf{m})\mathbf{H}(\mathbf{r}_0,t)\Big) = 0 \end{aligned} \tag{6}$$

Because $\mathbf{n}_{ax}$ and $\mathbf{m}$ are orthogonal, Eq. 6 is satisfied if the field vector is transverse to the screw axis, that is,

$$\mathbf{n}_{ax} \cdot \mathbf{H}(\mathbf{r}_0,t) = \mathbf{n}_{ax} \cdot \Big(\mathbf{G}\,\mathbf{r}_0 + \mathbf{H}_{offs}(t) + \mathbf{H}_{rot}(t)\Big) = 0 \tag{7}$$

Second, the torque should not fall below the minimum torque needed for actuation and should not change sign. For simplicity, we require a constant torque amplitude here. This requirement can be relaxed later on. A constant torque is provided by a field that rotates with constant angular velocity ω_c and constant strength $\|\mathbf{H}(\mathbf{r}_0, t)\| = H_c$ at the position of the screw so that

$$\|\mathbf{G}\,\mathbf{r}_0 + \mathbf{H}_{offs}(t) + \mathbf{H}_{rot}(t)\| = H_c \tag{8}$$

For actuation of a screw at position $\mathbf{r}_0$, the FFP is placed there by choosing

$$\mathbf{H}_{offs}(t) = -\mathbf{G}\,\mathbf{r}_0 \tag{9}$$

The time dependence of $\mathbf{H}_{offs}(t)$ indicates that, after actuation of one screw, the field is changed to move the FFP to the position of the next screw to be actuated. Placing the FFP at the screw position simplifies Eqs. 7 and 8 to

$$\mathbf{n}_{ax} \cdot \mathbf{H}_{rot}(t) = 0 \tag{10}$$

and

$$\|\mathbf{H}_{rot}(t)\| = H_c \tag{11}$$

respectively. To satisfy these requirements, the rotating field component can be written as

$$\mathbf{H}_{rot}(t) = H_c \begin{pmatrix} \cos\varphi(t)\sin\vartheta(t) \\ \sin\varphi(t)\sin\vartheta(t) \\ \cos\vartheta(t) \end{pmatrix} \tag{12}$$

where $\varphi(t)$ and $\vartheta(t)$ need to be chosen such that a rotation about the screw axis $\mathbf{n}_{ax}$ is realized with angular velocity ω. To this end, using Eq. 10, one angle can be removed, and depending on the orientation of $\mathbf{n}_{ax}$, the field can be parameterized by either $\varphi(t) = \omega t$ or $\vartheta(t) = \omega t$ (not detailed here).

In the presence of the static gradient field, application of a uniform field translates the FFP in space. The corresponding trajectory of the FFP can be obtained from the applied fields using Eqs. 1 and 3. In the xy plane, where the gradient strength is uniform, the rotating field makes the FFP move on a circle, as shown in Fig. 3 (A and B) and movie S3. However, a rotating field in the xz plane moves the FFP on an elliptical trajectory with a sense of rotation that is opposite to that of the local field vector, as displayed in Fig. 7 (A and B) and movie S5. If the screw axis is oriented perpendicularly to the xy or xz plane, the FFP trajectory lies in the respective plane. For all other orientations, the angle between the plane of FFP motion and the axis deviates from 90° and is determined by the polar angle θ of the screw axis in the laboratory frame (Fig. 2A). For $\theta = 54.7°$, the axis of rotation even lies in the plane of the FFP path. One example for an oblique axis with $\theta = 30°$ is displayed in Fig. 7 (C and D) and movie S6.

Spatial selection in 3D

From the field plots, one can derive that, if a screw is located above or below the plane of FFP motion, a tilting torque on its axis arises, which can be used to block the screw in a thread that is fixed in space. As described in the main text, the assumption of a minimal tilting torque magnitude necessary to block the screw leads to a cylinder-shaped actuation volume. Another criterion for blocking could be a minimal tilting angle that triggers blocking of the screw. In that case, the actuation volume becomes a double cone, whose projection is indicated by the red dashed lines in Figs. 3B and 7A.

Forces

For hard magnetic material, the magnitude of the magnetic moment of an object is constant, and the force acting on it depends on the gradient of the dot product between magnetic moment $\mathbf{m} = V\mathbf{M}$ and applied field $\mathbf{H}(\mathbf{r},t)$:

$$\mathbf{F}(\mathbf{r},t) = \mu_0 \nabla \left(\mathbf{m} \cdot \mathbf{H}(\mathbf{r},t) \right) \tag{13}$$

$$= \mu_0 VM \nabla \left(\hat{\mathbf{m}} \cdot \mathbf{H}(\mathbf{r},t) \right) \tag{14}$$

$\hat{\mathbf{m}}$ is a unit vector pointing in magnetization direction $\hat{\mathbf{m}} = \mathbf{m}/\|\mathbf{m}\| = (\hat{m}_x, \hat{m}_y, \hat{m}_z)^T$. V and $M = \|\mathbf{M}\|$ are volume and remanent magnetization magnitude of the magnetic material, respectively. If the orientation of the magnetic moment is fixed in space, the field configuration from Eq. 1 generates a constant force that depends on gradient strength and magnetic moment:

$$\mathbf{F}(\mathbf{r},t) = \mu_0 VM \nabla (\hat{\mathbf{m}} \cdot \mathbf{H}(\mathbf{r},t)) = \mu_0 VM \frac{G_z}{2} \begin{pmatrix} -\hat{m}_x \\ -\hat{m}_y \\ 2\hat{m}_z \end{pmatrix} \tag{15}$$

The offset and rotating field terms are uniform in space and thus disappear when applying the gradient operator. In the scenario of magnetic screws, the torque arising from applied fields will change the orientation of the magnetic moment and thus modulate the force. In contrast, magnetic swimmers would fully align their magnetic moment with the respective local field so that $\hat{\mathbf{m}} \cdot \mathbf{H}(\mathbf{r}, t) = \|\mathbf{H}(\mathbf{r}, t)\|$. In this case, calculation of the gradient of the field strength given by Eq. 4 introduces a dependence of the force on the polar angle ϑ of the vector between FFP and object:

$$\mathbf{F}(\mathbf{r}) = \mathbf{F}(r, \varphi, \vartheta)$$
$$= \mu_0 VM \frac{G_z}{2} \left(\mathbf{e}_r \sqrt{1 + 3\cos^2\vartheta} - \mathbf{e}_\vartheta \frac{3\cos\vartheta\sin\vartheta}{\sqrt{1 + 3\cos^2\vartheta}} \right) \tag{16}$$

$\mathbf{e}_r$ and $\mathbf{e}_\vartheta$ are unit vectors in radial and polar direction, respectively. This force for objects aligned with the field presents the upper limit of forces that can act on arbitrarily oriented objects. The force magnitude is maximal when the object's magnetic moment is aligned in z direction ($\vartheta = 0°$), that is, the strong gradient direction. When changing the orientation toward the xy plane, it decreases by a factor of 2.

As an example, consider an NdFeB sphere of diameter $d = {}^1/_3$ mm with remanent magnetization $M = 1.0\ \mathrm{T}/\mu_0$. The maximum field gradient that can be achieved in a patient with reasonable effort is probably around $G_z = 2.0\ \mathrm{T/m}/\mu_0$. In that case, the maximum force would be

$$F_{\max} = \mu_0 \frac{\pi}{6} d^3 M G_z$$
$$= \frac{1}{4\pi \cdot 10^{-7}} \cdot \frac{\pi}{6} \cdot \frac{1}{27} \cdot 10^{-9} \cdot 2.0\ \mathrm{A^2 m^2 T^2/N} \approx 30.9\ \mu\mathrm{N} \tag{17}$$

The weight of the same sphere would be

$$F_{\text{weight}} = g\rho \frac{\pi}{6} d^3$$
$$= 9.81 \cdot 7.4 \cdot \frac{\pi}{6} \cdot \frac{1}{27} \cdot 10^{-9}\ \mathrm{m/s^2\ g/cm^3\ m^3} \approx 1.4\ \mu\mathrm{N} \tag{18}$$

where $g = 9.81\ \mathrm{m/s^2}$ is the acceleration due to gravity and $\rho = 7.4\ \mathrm{g/cm^3}$ is the density of NdFeB. In the case of a magnetically switchable seed, the magnetic material represents only a small part of the device so that the force should be related to the weight of the seed. A typical seed has a length of 4.5 mm, a diameter of 0.9 mm, and a weight of 10 mg (*36*), that is, about 100 μN. Thus, if magnetic material comparable to the volume of the abovementioned sphere were used to drive the screw, then the maximum magnetic force on a seed would be smaller than its weight.

Field generators and achievable spatial selectivity

Two different field generators were used for experimental verification. Both were built for generating the gradient and offset fields necessary for spatial encoding in MPI (*18*). One system ("preclinical demonstrator"; Fig. 1, A and B) achieves a maximum gradient strength of $G_z = 2.5\ \mathrm{T/m}/\mu_0$ in the vertical direction and half this value in the planar directions ($G_x = G_y = -G_z/2$). It can generate uniform fields of up to $100\ \mathrm{mT}/\mu_0$ for applying dynamic sequences, for example, for screw rotation and for shifting the FFP inside the bore, which has a diameter of 12 cm (*20*). A larger system ("clinical demonstrator"; Fig. 5, A and B) has an elliptical bore with diameters of 34 cm and 45 cm in vertical and horizontal direction, respectively. The field applicator consists of 16 coil stacks with soft magnetic cores, which can be operated via 16 independent amplifiers to generate the desired field configurations. It can maintain a gradient strength of $G_z = 2.0\ \mathrm{T/m}/\mu_0 = 2G_x = 2G_y$ while the FFP is moved over a spherical volume of diameter 20 cm (*19*). If no gradient field is applied, it achieves maximum uniform field strengths of about $100\ \mathrm{mT}/\mu_0$ and $400\ \mathrm{mT}/\mu_0$ in horizontal and vertical direction, respectively. On both systems, all fields can be switched rapidly, although switching is limited by eddy-current effects. Depending on field amplitude, rotational fields with frequencies between a few hertz and more than 100 Hz can be applied.

For a conservative estimate of the achievable spatial selectivity, we require a minimal field strength $H_{\text{rot,min}}$ to drive the desired screw, whereas neighboring screws are assumed to turn freely at any nonzero field strength. In that case, the spatial selectivity Δr corresponds to the FFP path radius for the maximum gradient strength that can be applied: $r_{\text{FFP,min}} = H_{\text{rot,min}}/G_{x,\max}$. For reliable operation of our screw prototypes, we estimate a minimal field of $H_{\text{rot,min}} = 4\ \mathrm{mT}/\mu_0$, which, for the preclinical field applicator, would lead to a spatial selectivity, or minimal required screw separation, of $\Delta r = 3.2$ mm in horizontal direction ($G_x = G_y = 1.25\ \mathrm{T/m}/\mu_0$).

For an estimation of the vertical selectivity, we approximate the screw by a cylindrical object of length l and diameter d, which is located inside a slightly larger hollow cylinder representing the thread. The magnetic field component parallel to the screw axis, $\mathbf{H}_{\text{tilt}}$, then

applies a tilting torque that presses the inner cylinder to the outer cylinder at two contact points. By calculating the force on the contact points, one can derive a friction force, which depends on the static coefficient of friction μ_s. The resulting frictional torque now has to be larger than the rotational torque to lock the screw. Assuming that the rotational field component $\mathbf{H}_{rot}$ is applied perpendicularly to the screw axis, one can derive the following relation:

$$\|\mathbf{H}_{tilt}\| > \frac{l}{\mu_s d}\|\mathbf{H}_{rot}\| \quad (19)$$

Using typical values $l = 3$ mm, $d = 2$ mm, and $\mu_s = 1$, one finds that the prefactor is of the order of unity, and thus, the fields have to be of similar magnitude. Depending on orientation with respect to the gradient system, spatial selectivity may vary by an additional factor of 2 between the directions parallel and transverse to the screw axis.

SUPPLEMENTARY MATERIALS

robotics.sciencemag.org/cgi/content/full/2/3/eaal2845/DC1
Fig. S1. Amplifier current sequence used for actuation in movies S9 and S10.
Movie S1. Demonstration of spatially selective actuation.
Movie S2. Experimental verification of horizontally selective actuation.
Movie S3. Field configuration for driving a vertically aligned screw.
Movie S4. Experimental verification of vertically selective actuation.
Movie S5. Field configuration for driving a horizontally aligned screw (along *y* axis).
Movie S6. Field configuration for driving an obliquely aligned screw.
Movie S7. Demonstration of spatially selective actuation on clinical-scale field applicator.
Movie S8. Mechanism based on five selectively actuated screws (front view).
Movie S9. Mechanism based on five selectively actuated screws (back view).

REFERENCES AND NOTES

1. S. Ernst, F. Ouyang, C. Linder, K. Hertting, F. Stahl, J. Chun, H. Hachiya, D. Bänsch, M. Antz, K.-H. Kuck, Initial experience with remote catheter ablation using a novel magnetic navigation system: Magnetic remote catheter ablation. *Circulation* **109**, 1472–1475 (2004).
2. G. Ciuti, A. Menciassi, P. Dario, Capsule endoscopy: From current achievements to open challenges. *IEEE Rev. Biomed. Eng.* **4**, 59–72 (2011).
3. O. Cugat, J. Delamare, G. Reyne, Magnetic micro-actuators and systems (MAGMAS). *IEEE Trans. Magn.* **39**, 3607–3612 (2003).
4. D. Walker, B. T. Käsdorf, H.-H. Jeong, O. Lieleg, P. Fischer, Enzymatically active biomimetic micropropellers for the penetration of mucin gels. *Sci. Adv.* **1**, e1500501 (2015).
5. J. J. Abbott, K. E. Peyer, M. C. Lagomarsino, L. Zhang, L. Dong, I. K. Kaliakatsos, B. J. Nelson, How should microrobots swim? *Int. J. Rob. Res.* **28**, 1434–1447 (2009).
6. R. Dreyfus, J. Baudry, M. L. Roper, M. Fermigier, H. A. Stone, J. Bibette, Microscopic artificial swimmers. *Nature* **437**, 862–865 (2005).
7. W. Gao, D. Kagan, O. S. Pak, C. Clawson, S. Campuzano, E. Chuluun-Erdene, E. Shipton, E. E. Fullerton, L. Zhang, E. Lauga, J. Wang, Cargo-towing fuel-free magnetic nanoswimmers for targeted drug delivery. *Small* **8**, 460–467 (2012).
8. S. Y. Chin, Y. C. Poh, A.-C. Kohler, J. T. Compton, L. L. Hsu, K. M. Lau, S. Kim, B. W. Lee, F. Y. Lee, S. K. Sia, Additive manufacturing of hydrogel-based materials for next-generation implantable medical devices. *Sci. Robot.* **2**, eaah6451 (2017).
9. T. Qiu, T.-C. Lee, A. G. Mark, K. I. Morozov, R. Münster, O. Mierka, S. Turek, A. M. Leshansky, P. Fischer, Swimming by reciprocal motion at low Reynolds number. *Nat. Commun.* **5**, 5119 (2014).
10. P. J. Vach, D. Faivre, The triathlon of magnetic actuation: Rolling, propelling, swimming with a single magnetic material. *Sci. Rep.* **5**, 9364 (2015).
11. K. E. Peyer, S. Tottori, F. Qiu, L. Zhang, B. J. Nelson, Magnetic helical micromachines. *Chemistry* **19**, 28–38 (2013).
12. B. J. Nelson, I. K. Kaliakatsos, J. J. Abbott, Microrobots for minimally invasive medicine. *Annu. Rev. Biomed. Eng.* **12**, 55–85 (2010).
13. A. Servant, F. Qiu, M. Mazza, K. Kostarelos, B. J. Nelson, Controlled in vivo swimming of a swarm of bacteria-like microrobotic flagella. *Adv. Mater.* **27**, 2981–2988 (2015).
14. E. Diller, M. Sitti, Micro-scale mobile robotics. *Found. Trends Robot.* **2**, 143–259 (2011).
15. S. Tottori, N. Sugita, R. Kometani, S. Ishihara, M. Mitsuishi, Selective control method for multiple magnetic helical microrobots. *J. Micro-Nano Mechatron.* **6**, 89–95 (2011).
16. E. Diller, J. Giltinan, M. Sitti, Independent control of multiple magnetic microrobots in three dimensions. *Int. J. Rob. Res.* **32**, 614–631 (2013).
17. A. W. Mahoney, N. D. Nelson, K. E. Peyer, B. J. Nelson, J. J. Abbott, Behavior of rotating magnetic microrobots above the step-out frequency with application to control of multi-microrobot systems. *Appl. Phys. Lett.* **104**, 144101 (2014).
18. B. Gleich, J. Weizenecker, Tomographic imaging using the nonlinear response of magnetic particles. *Nature* **435**, 1214–1217 (2005).
19. J. Borgert, J. D. Schmidt, I. Schmale, J. Rahmer, C. Bontus, B. Gleich, B. David, R. Eckart, O. Woywode, J. Weizenecker, J. Schnorr, M. Taupitz, J. Haegele, F. M. Vogt, J. Barkhausen, Fundamentals and applications of magnetic particle imaging. *J. Cardiovasc. Comput. Tomogr.* **6**, 149–153 (2012).
20. N. Nothnagel, J. Rahmer, B. Gleich, A. Halkola, T. M. Buzug, J. Borgert, Steering of magnetic devices with a magnetic particle imaging system. *IEEE Trans. Biomed. Eng.* **63**, 2286–2293 (2016).
21. J. C. Maxwell, *A Treatise on Electricity and Magnetism* (Clarendon Press, 1873).
22. J. L. Prince, J. Links, *Medical Imaging Signals and Systems* (Prentice Hall, 2014).
23. E. C. Halperin, L. W. Brady, D. E. Wazer, C. A. Perez, *Perez and Brady's Principles and Practice of Radiation Oncology* (Lippincott Williams & Wilkins, 2013).
24. K. Ishiyama, M. Sendoh, A. Yamazaki, M. Inoue, K. I. Arai, Swimming of magnetic micro-machines under a very wide-range of Reynolds number conditions. *IEEE Trans. Magn.* **37**, 2868–2870 (2001).
25. A. Collo, P. Poignet, C. Hamitouche, S. Almouahed, E. Stindel, *2014 36th Annual International Conference of the IEEE Engineering in Medicine and Biology Society (EMBC 2014)*, Chicago, IL, 26 to 30 August 2014.
26. R. Kotz, R. Windhager, M. Dominkus, B. Robioneck, H. Müller-Daniels, A self-extending paediatric leg implant. *Nature* **406**, 143–144 (2000).
27. Z. Dannawi, F. Altaf, N. S. Harshavardhana, H. El Sebaie, H. Noordeen, Early results of a remotely-operated magnetic growth rod in early-onset scoliosis. *Bone Joint J.* **95-B**, 75–80 (2013).
28. D. A. LaVan, T. McGuire, R. Langer, Small-scale systems for in vivo drug delivery. *Nat Biotechnol.* **21**, 1184–1191 (2003).
29. L. Lin, R. R. Patel, B. R. Thomadsen, D. L. Henderson, The use of directional interstitial sources to improve dosimetry in breast brachytherapy. *Med. Phys.* **35**, 240–247 (2008).
30. V. Chaswal, B. R. Thomadsen, L. Lin, D. L. Henderson, Interstitial prostate implant brachytherapy using an automated, 3-D greedy heuristic optimization and I-125 directional sources. *Brachytherapy* **6**, 78 (2007).
31. P. Hass, K. Mohnike, Extending the frontiers beyond thermal ablation by radiofrequency ablation: SBRT, brachytherapy, SIRT (radioembolization). *Viszeralmedizin* **30**, 245–252 (2014).
32. J. Weizenecker, B. Gleich, J. Rahmer, H. Dahnke, J. Borgert, Three-dimensional real-time in vivo magnetic particle imaging. *Phys. Med. Biol.* **54**, L1–L10 (2009).
33. J. Haegele, S. Vaalma, N. Panagiotopoulos, J. Barkhausen, F. M. Vogt, J. Borgert, J. Rahmer, Multi-color magnetic particle imaging for cardiovascular interventions. *Phys. Med. Biol.* **61**, N415–N426 (2016).
34. J. Haegele, N. Panagiotopoulos, S. Cremers, J. Rahmer, J. Franke, R. L. Duschka, S. Vaalma, M. Heidenreich, J. Borgert, P. Borm, J. Barkhausen, F. M. Vogt, Magnetic particle imaging: A resovist based marking technology for guide wires and catheters for vascular interventions. *IEEE Trans. Med. Imag.* **35**, 2312–2318 (2016).
35. S. S. Hidalgo-Tobon, Theory of gradient coil design methods for magnetic resonance imaging. *Concepts Magn. Reson.* **36A**, 223–242 (2010).
36. A. Sugawara, J. Nakashima, E. Kunieda, H. Nagata, R. Mizuno, S. Seki, Y. Shiraishi, R. Kouta, M. Oya, N. Shigematsu, Incidence of seed migration to the chest, abdomen, and pelvis after transperineal interstitial prostate brachytherapy with loose ^{125}I seeds. *Radiat. Oncol.* **6**, 130 (2011).

Acknowledgments: We thank the MPI team for building the field applicators. We also thank J. Weizenecker and U. Heinen for helpful discussions. **Funding:** We acknowledge funding by the German Federal Ministry of Education and Research under the grant numbers 13GW0069C and 13N11086. **Author contributions:** J.R. derived the math, implemented the actuation sequences, and wrote the manuscript. B.G. conceived the idea of switchable radioactive seeds and built the demonstrator seeds. C.S. supported the experiments and created part of movies. **Competing interests:** J.R. and B.G. are employees of Philips GmbH Innovative Technologies, Research Laboratories Hamburg, Germany. C.S. is an employee of Philips GmbH Market DACH, Hamburg, Germany. All authors are co-inventors on patent application EP16160684.3 submitted by Koninklijke Philips N.V. that covers the concept of and devices for spatially selective magnetic manipulation including the application in switchable radioactive seeds. **Data and materials availability:** Correspondence and requests for materials should be addressed to J.R. (juergen.rahmer@philips.com).

Submitted 26 October 2016
Accepted 26 January 2017
Published 15 February 2017
10.1126/scirobotics.aal2845

Citation: J. Rahmer, C. Stehning, B. Gleich, Spatially selective remote magnetic actuation of identical helical micromachines. *Sci. Robot.* **2**, eaal2845 (2017).

Science Robotics

Spatially selective remote magnetic actuation of identical helical micromachines

Jürgen Rahmer, Christian Stehning, and Bernhard Gleich

Sci. Robot. **2** (3), eaal2845. DOI: 10.1126/scirobotics.aal2845

Science Robotics (ISSN 2470-9476) is published by the American Association for the Advancement of Science. 1200 New York Avenue NW, Washington, DC 20005. The title *Science Robotics* is a registered trademark of AAAS.